Supplementary Information

Machine Learning-Assisted 3D Printing of Thermoelectric Materials of Ultrahigh Performances at Room Temperature

Kaidong Song,[‡a] Guoyue Xu,[‡a] Ali Newaz Mohammad Tanvir,[‡a] Ke Wang,[b] Md Omarsany Bappy,[a] Haijian Yang,[c] Wenjie Shang,[a] Le Zhou,[c] Alexander W. Dowling,[b] Tengei Luo[*a] and Yanliang Zhang[*a]

([+]These authors made equal contributions)

[a.] *Department of Aerospace and Mechanical Engineering, University of Notre Dame, Notre Dame, IN 46556, USA. E-mail: tluo@nd.edu; yzhang45@nd.edu*

[b.] *Department of Chemical and Biomolecular Engineering, University of Notre Dame, Notre Dame, IN 46556, USA.*

[c.] *Department of Mechanical Engineering, Marquette University, Milwaukee, WI 53233, USA.*

Contents

Supplementary Note 1. Ink appearance with modification

To enhance the printability of BiSbTe-based thermoelectric ink, Xanthan gum (X-gum) was incorporated to adjust the ink viscosity and yield stress. This modification is illustrated in **Figure S1**, where the addition of X-gum led to the solvent transitioning from a liquid to a solid state. Consequently, the ink itself also becomes solid when at rest. Furthermore, overhang filaments were printed to examine the ink's structural stability. As depicted in **Figure S1b**, the rheological modified ink successfully formed filaments with precise geometry on a support structure. When these filaments were extruded beyond the support, the modified ink quickly changed from a liquid-like to a solid-like state, facilitated by its yield stress and shear-thinning properties. This resulted in forming rigid filaments capable of retaining their shape in mid-air. In contrast, filaments made with unmodified ink, as shown in **Figure S1a**, lacked enough yield stress to support the printed spanning structures. This ability to print self-supporting filaments demonstrates the effectiveness of X-gum modification, indicating its suitability for creating complex 3D structures through printing.
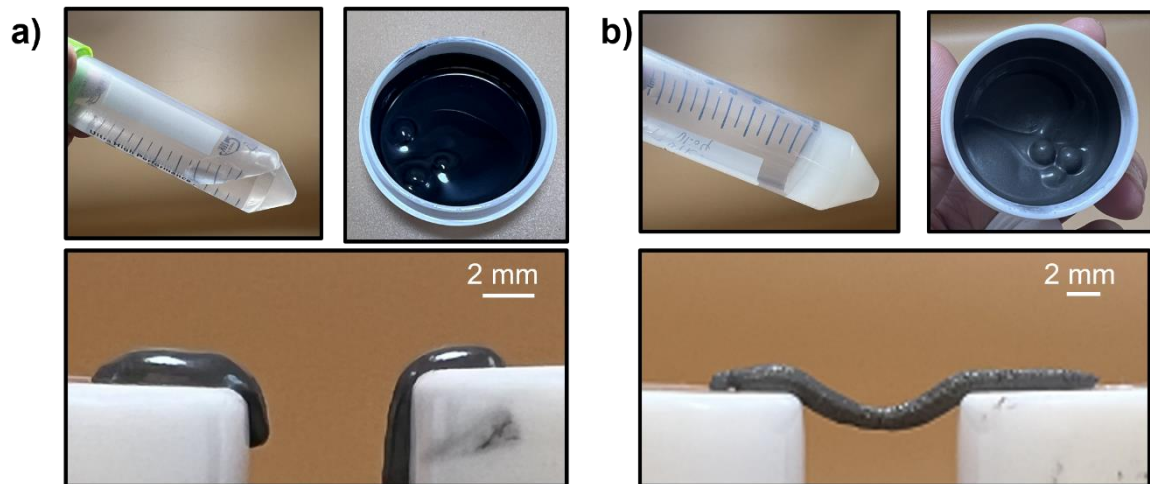

Figure S1. Ink appearance (a) before and (b) after modification with X-gum.

Supplementary Note 2. Ink rheological properties

Figures S2a and **S2b** illustrate that both X-gum-modified and unmodified inks are shear-thinning non-Newtonian fluids, meaning their viscosity decreases as the shear rate increases. This shear-thinning property occurs because, under shear stress (like stirring or extrusion), X-gum's molecular chains align in the flow direction, reducing internal resistance and lowering viscosity, thus enabling more effortless fluid flow. When the shear force is removed, X-gum molecules return to a disordered state, and the ink regains its initial viscosity. This reversible viscosity change under different shear rates makes X-gum an ideal component in ink formulations for precise, clean printing, as it flows easily under printing stress but thickens afterward to prevent spreading.

In addition to being shear-thinning, the thermoelectric (TE) inks exhibit viscoelasticity with yield stress, as shown in **Figures S2c** and **S2d**. The yield stress increases with a higher concentration of X-gum due to X-gum's ability to form a weak gel-like network in the solution that traps solvent molecules, imparting a solid-like behavior under low shear. When shear stress surpasses the yield stress, the network breaks down, and the ink flows. This characteristic is crucial for 3D printing, where the ink must stay stable and retain shape when at rest or under low stress but flow readily when extruded. The ink's viscosity increases post-extrusion, aiding in maintaining the structure of the print. Moreover, higher particle loading leads to increased yield stress, as seen in the comparison between 62 and 82 wt.% particle loadings, due to more particles being jammed together.
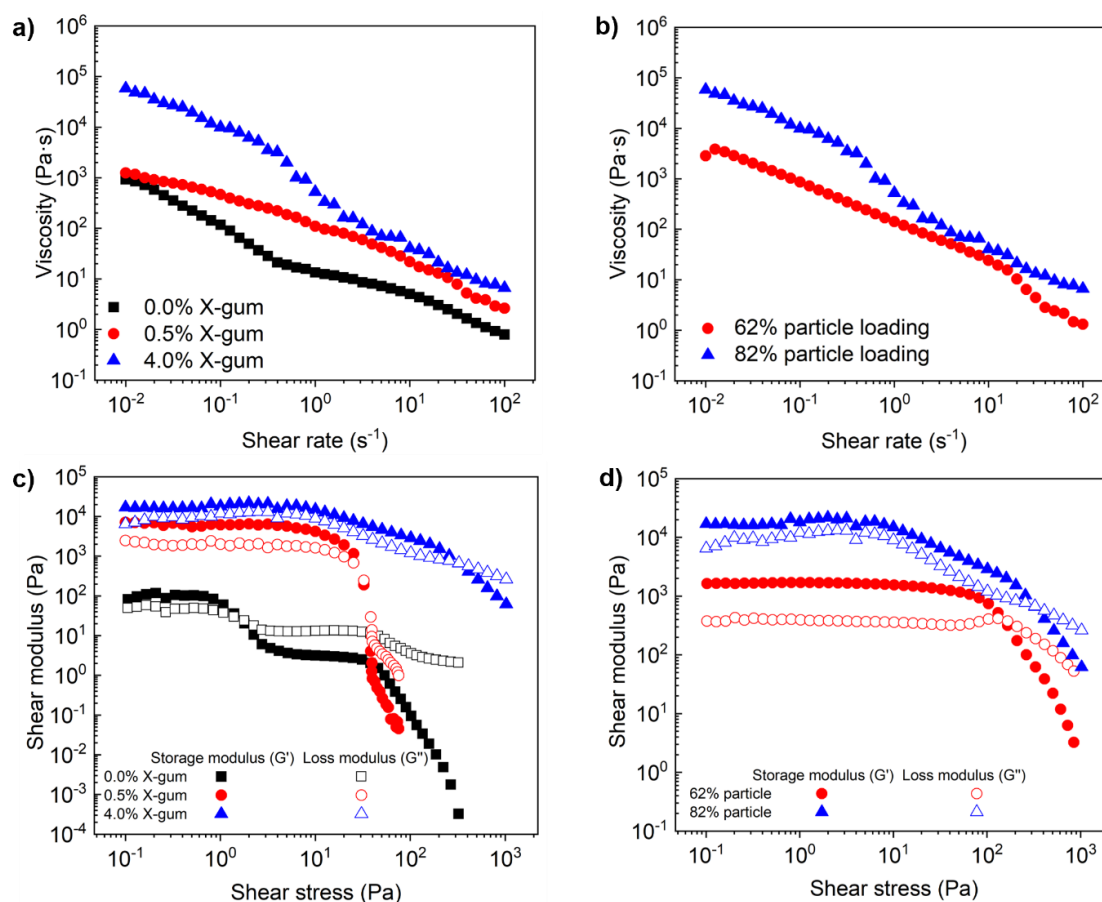

Figure S2. Rheological data of TE. (a) (b) Viscosity versus shear rate with a log scale and, (c) (d) shear moduli as a function of shear stress.

Supplementary Note 3. Machine learning process

Figure S3 visulaized the input and output from the machine learning model, aiming to solve a co-optimization problem for identifying the optimal combination of ink formulation with printing conditions that will maximize the thermoelectric power factor with constraints of 3D filament uniformity and structure surface roughness. The model takes both ink and process parameters: the former controls the concentration of X-gum and BiSbTe (TE) particle loading, while the latter includes the standoff distance and filament spacing. The machine learning model assimilates those multi-dimensional variables to predict the corresponding power factor as well as filament uniformity and structural roughness coefficient. Those predicted values will be leveraged by Bayesian optimization (BO) algorithms to recommend new experimental conditions, refining the search for optimal parameters through the iterative learning strategy.

Input properties

Ink Parameters
- TE particle loading (wt %): x_1
- X-gum concentration (wt %) : x_2

Process Parameters
- Fialment spacing (mm): x_3
- Standoff distance (mm): x_4

Evaluate metrics

TE Property
- Power factor (µW/mK^2): y_1

Printability
- Filament uniformity: y_2
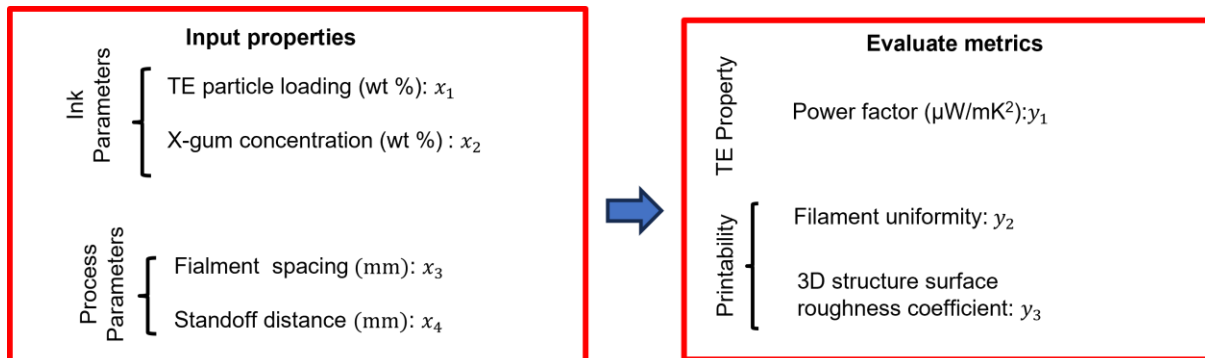- 3D structure surface roughness coefficient: y_3

Figure S3. Input parameters and evaluate metrics for machine learning.

Supplementary Note 4. Properties evaluation criteria

As illustrated in **Figure S4a**, there are four types of filament morphology, and the filament morphology may eventually change from well-defined to irregular to broken. A dimensionless number defined as filament uniformity (y_2) was used to quantify the morphology of filaments by calculating the ratio of the pixel area of a printed filament over the total pixel area of an ideally deposited filament (the area inside the dashed rectangle) (**Equation S1**). Photographic images of each printed filament were analyzed using ImageJ (NIH, Bethesda, Maryland) to yield the values of pixel area to determine y_2.

Figure S4b illustrates the effects of filament spacing and the representative surface roughness measurement figures. During extrusion printing, a subsequently deposited filament overlaps with a previously deposited filament. If the overlap distance is too large, the whole structure may have poor integrity and large surface roughness due to the weak connection between adjacent filaments. If the overlap distance is too small, the subsequently printed filament overlaps with the previously deposited filament, and the resulting over-deposition phenomenon can be evident. The overlap distance must be carefully selected to ensure the structure has enough integrity and minimizes the over-deposition phenomenon and surface roughness. A suitable overlap should make a printed structure with a good fusion between filaments, which results in good mechanical strength and low surface roughness. The calculation of this 3D structure roughness coefficient can be found in **Equation S2**.

$$\text{Filament uniformity ratio } (y_2) = \frac{\text{pixel area of a printed filament}}{\text{pixel area of a perfectly deposited filament}} \text{ (\textbf{Equation S1})}$$

$$\text{3D structure roughness coefficient } (y_3) = \frac{\text{arithmetic average roughess } (Ra)}{\text{filament diameter}} \text{ (\textbf{Equation S2})}$$

a) Standoff distance:

Small distance　　Suitable distance　　Large distance　　Too large distance

b) Filament Spacing:

Narrow filament spacing　　Suitable filament spacing　　Large filament spacing
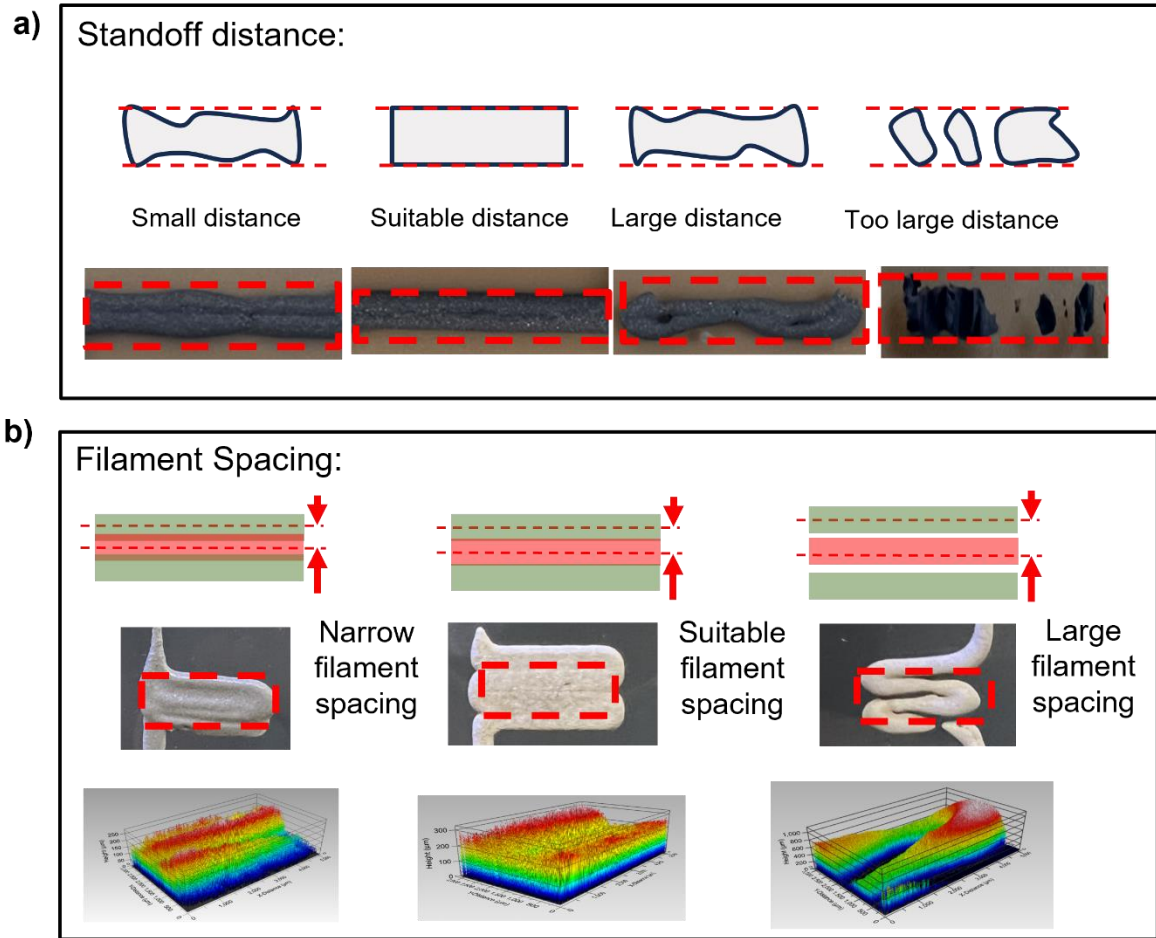
Figure S4. Properties evaluation criteria for (a) standoff distance and (b) filament spacing.

Supplementary Note 5. All experimental data

Table S1 provides detailed experimental data for all four rounds. **Table S2** compares the power factor for samples created using various 3D printing techniques.

Table S1. Experimental and machine learning database for printing BiSbTe ink

Round	Exp #	Solid phase ratio (wt %)	X-gum concentration (wt %)	Standoff distance (mm)	Line distance (mm)	Power factor ($\mu W/mK^2$)	Power factor_std ($\mu W/mK^2$)	Filament uniformity (N/A)	Filament_std (N/A)	3D roughness coefficient (%)	3D_std (%)
0	1	42	4.00	0.75	1.4	133.80	20.89	0.897	0.009	6.847	0.998
0	2	42	2.00	0.75	2.0	242.27	84.35	0.938	0.006	1.740	0.172
0	3	42	1.00	0.75	1.4	311.97	54.15	0.784	0.009	3.434	0.986
0	4	62	4.00	0.75	1.4	634.71	110.81	0.788	0.035	4.875	2.139
0	5	62	2.00	0.75	1.4	1719.88	198.32	0.830	0.062	3.130	0.659
0	6	62	2.00	1.54	1.4	1655.85	13.19	0.928	0.013	3.121	0.004
0	7	62	2.00	1.54	1.0	1710.73	44.19	0.928	0.013	3.484	0.611
0	8	62	2.00	1.54	2.0	1568.91	9.55	0.928	0.013	7.614	0.537
0	9	62	1.00	0.30	1.4	2034.92	152.18	0.817	0.025	3.868	0.125
0	10	62	1.00	0.75	1.4	2074.51	171.53	0.922	0.026	2.781	0.250
0	11	62	1.00	1.00	1.4	1982.31	167.72	0.937	0.013	2.775	0.714
0	12	62	1.00	1.00	1.0	2132.95	225.92	0.937	0.013	4.290	0.012
0	13	62	1.00	1.00	2.0	2061.15	43.79	0.937	0.013	1.785	0.056
0	14	69	1.00	0.30	2.0	2349.56	359.00	0.823	0.028	4.223	0.545
0	15	82	1.00	2.00	2.0	2332.41	25.34	0.863	0.088	6.760	1.449
1	16	75	0.50	1.00	1.5	2513.65	322.57	0.808	0.034	3.555	0.273
1	17	82	0.70	1.20	1.4	3004.75	193.30	0.848	0.009	2.249	0.368
1	18	80	0.50	1.00	1.5	2997.06	71.88	0.810	0.056	2.795	0.055
2	19	82	0.50	1.50	1.0	3010.33	171.04	0.860	0.005	2.275	0.248
2	20	84	0.50	1.50	1.0	2688.41	99.48	0.753	0.057	2.753	0.190
2	21	84	0.50	1.10	1.0	2718.77	350.18	0.723	0.027	2.849	0.313
3	22	83	0.50	1.00	1.6	3014.06	223.17	0.824	0.028	2.468	0.198
3	23	83	0.70	1.00	1.6	2982.73	110.81	0.835	0.010	2.564	0.540
3	24	81	0.50	1.00	1.6	2987.51	83.62	0.840	0.024	3.000	0.288

Table S2. Comparison of printing methods

Active material	Additives	Process	Power factor ($\mu W/mK^2$)	zT	Ref
$Bi_{0.4}Sb_{1.6}Te_3$		Screen printing	~3000	1.0	[1]
$Bi_xSb_{2-x}Te_3$	Chalcogenidometallate (ChaM)	Extrusion printing	~2400	~0.95	[2]
$Ag_{2.1}Te$		Inkjet printing	~222.5	0.19	[3]
PEDOT:PSS	Multiwall carbon nanotubes	Aerosol jet printing	~20	0.022	[4]
$Bi_{0.4}Sb_{1.6}Te_3$	X-gum	Extrusion printing	~3000	1.3	This work

Supplementary Note 6. Correlations analysis

In **Figure S6a**, it has been shown that there is a positive correlation (0.928), between TE particle loading (solid phase ratio) and thermoelectric power factor. Notably, beyond an 83% threshold, the incremental benefits begin to diminish markedly. In **Figure S6b**, a reduction in the additive (Xanthan gum) concentration has been associated with an enhancement in power factor, displaying a correlation factor of 0.791, with diminishing marginal returns below 0.7%. It is important to recognize that lowering the X-gum concentration below this point can negatively affect printability and reduce the quality of the filament and roughness, with the roughness nearing the maximum limit we find acceptable, as evidenced in **Figures S6c** and **S6d**. Consequently, the empirical evidence guided the cessation of further increases in solid phase ratio at 84% and X-gum concentration at 0.5%. The observed correlations confirm the presence of non-linear relationships among variables.
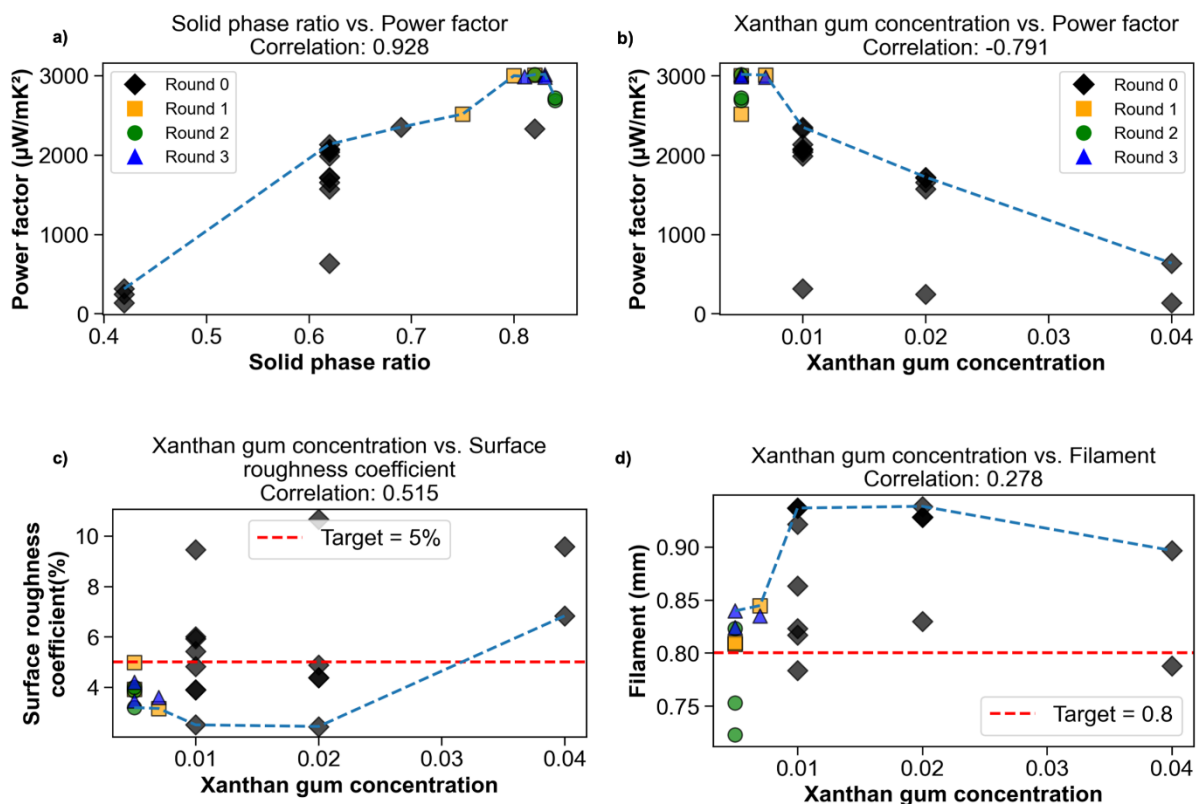

Figure S6. Data correlation analysis. (a) Solid phase ratio and power factor correlation. (b) X-gum concentration and power factor correlation. (c) X-gum and roughness correlation. (d) X-gum and filament correlation.

Supplementary Note 7. Candidate selection informed by constrained BO

Note 7 describes the process for selecting candidates. **Figure S7a** shows the mean of the GPR predictions as a function of TE particle loading ratio and additive (X-gum) concentration. Standoff distance is fixed at 1 mm, and filament spacing is fixed at 1.6 mm. The hollow diamond symbols mean the projection of the experimental data to this plane, and the green stars mean the points chosen for the next round of the experiment. Similarly, **Figure S7b** shows the uncertainty of the GPR predictions. The blue regions are denoted as the zones that have been thoroughly explored, suggesting a shift in strategy towards the exploitation of these areas. **Figure S7c** shows the Expected Improvement (EI) metric, where it shows the potential increment. **Figure S7d** shows the constrained EI, highlighting the most favorable region for achieving high power factors while within the set constraints, which is determined by the product of the SVMs probabilities and the EI value. Compared to **Figure S7c**, the red region shrinks, balancing on the regions where high power factor and material printability are both achievable. The red areas in this figure reflect the most favorable conditions recommended for future experiments, balancing the maximization of the power factor against the practical limitations of material printability.

By including the expert intuition in the selection, the highest constrained EI point was selected, and two more points around the red region for exploration. The effectiveness of this region was confirmed through experimentation, leading to the attainment of significant power factors, approximately 3000 $\mu W/mK^2$, and creating structures with a mean roughness coefficient of 0.025.
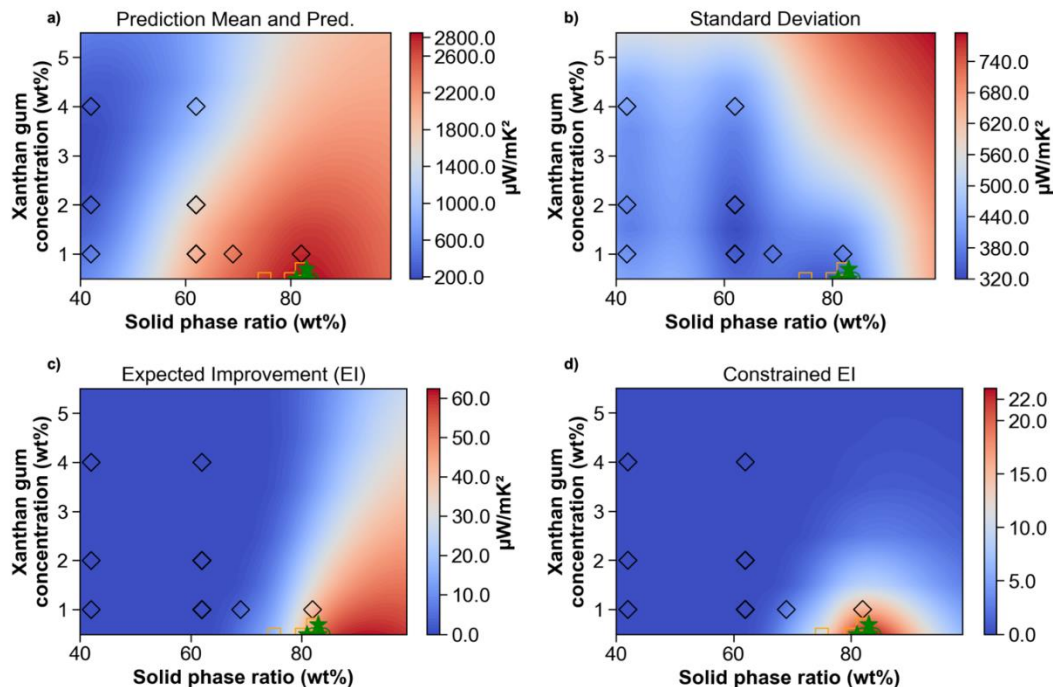

Figure S7. The cross-section figure at standoff distance at 1mm and line distance at 1.6mm. The hollow points are the projection points in this cross-section. The stars represent the candidates for the next round of experiments. a) the GPR prediction means. b) the GPR prediction standard deviations c) the expected improvement BO. d) the constrained Expected Improvement.

Supplementary Note 8. SEM and EDS of unoptimized sample

An analysis of scanning electron microscopy (SEM) and energy-dispersive X-ray spectroscopy (EDS) is conducted on polished cross-sections (surface horizontal to the pressing direction) of printed samples using unoptimized inks (**Figure S8**).
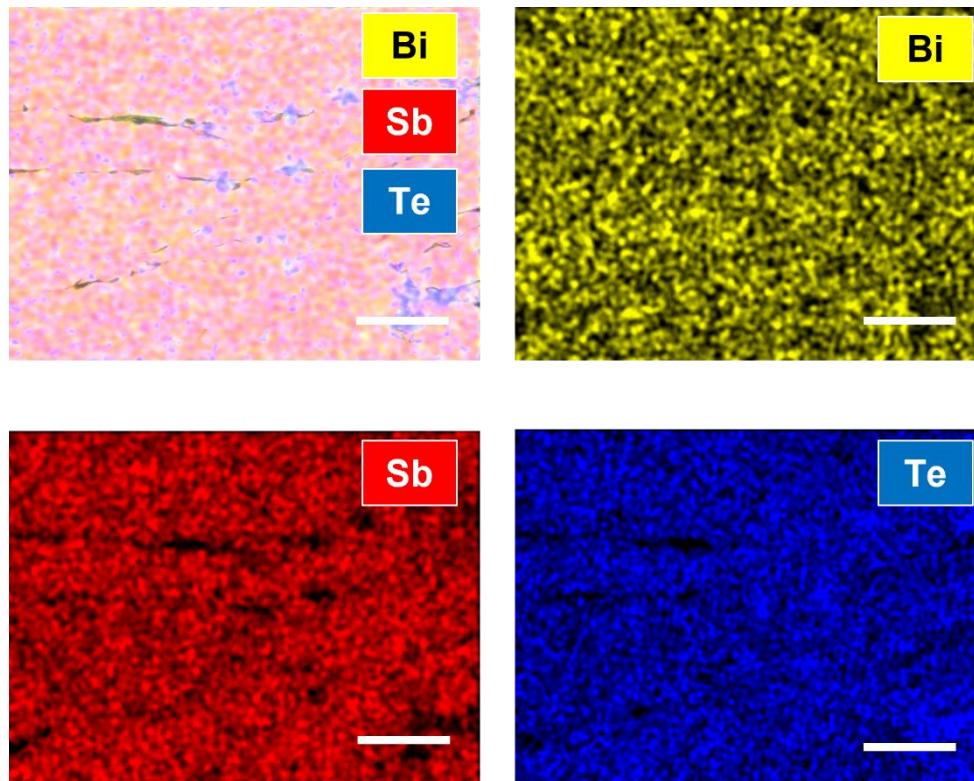

Figure S8. Cross-sectional EDS images of samples printed through unoptimized ink.

Supplementary Note 9. Cross-section SEM of sample processed by HIP

The microstructure of printed TE samples before and after hot isostatic pressing (HIP) is shown in **Figure S9**.
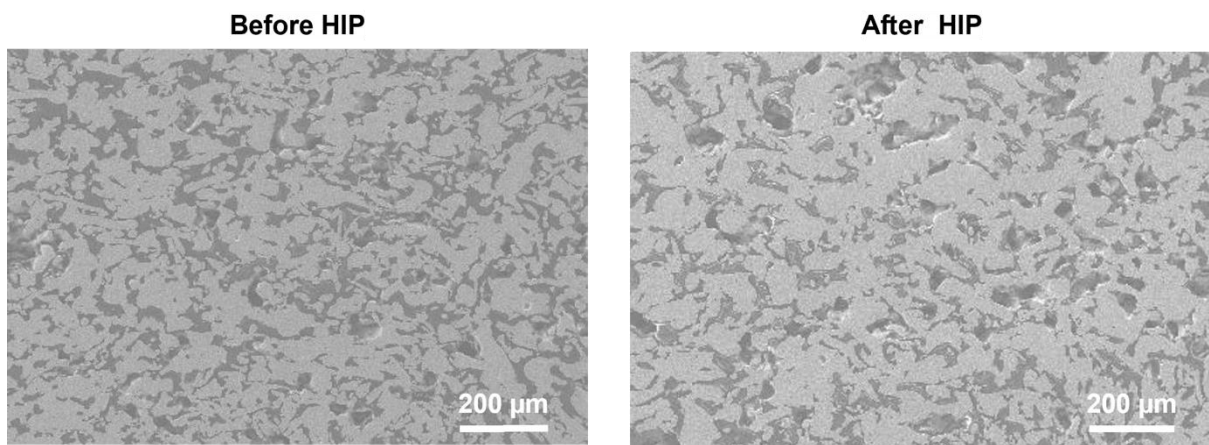

Figure S9. Cross-sectional SEM images of printed samples before and after HIP.

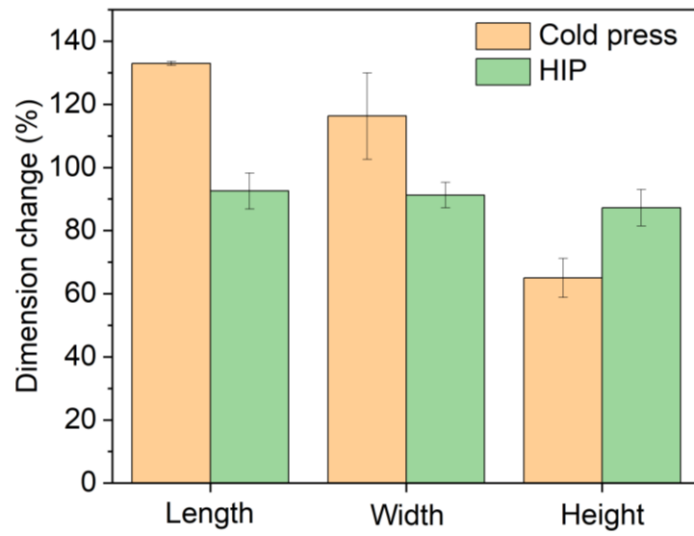**Supplementary Note 10. Dimensional change evaluation**

Figure S10. Comparison of samples dimension change under cold press and HIP conditions.

Supplementary Note 11. Thermal conductivity measurement

The optimized BiSbTe sample's in-plane thermal diffusivity is measured using the Angstrom technique.[5] The function generator (RIGOL DG4062) generates a periodic heat signal at one end of the film for this measurement in vacuum (~2 mTorr). A data acquisition device (Keysight 34970A) is used to measure the amplitude and phase of the resulting temperatures at two points along the sample. Two commercial k-type thermocouples (Omega, 5TC 40 AWG) are used to record the temperature; one is placed close to the heater and the other is placed farther away. To ensure a significant temperature oscillation at the far end of the sample, the frequency range is selected so that the thermal penetration depth is as large as possible while remaining smaller than the distance between the two thermocouples. The following equation is used to compute thermal diffusivity (α):

$$\alpha = \frac{L^2}{2dt\ln\frac{A_1}{A_2}}$$

where A_1 and A_2 represent the temperature phase difference and amplitudes at the near-side and far-side locations, respectively, and L denotes the distance between the two thermocouples.

The formula, $k = \alpha\rho c_p$ where α, c_p, and ρ represent thermal diffusivity, specific heat, and density, respectively, can be used to calculate thermal conductivity (κ) from the measured thermal diffusivity (α), specific heat capacity (c_p), and density (ρ). **Figure S11** shows the variation in temperature amplitude for thermocouples located on the near and far sides.
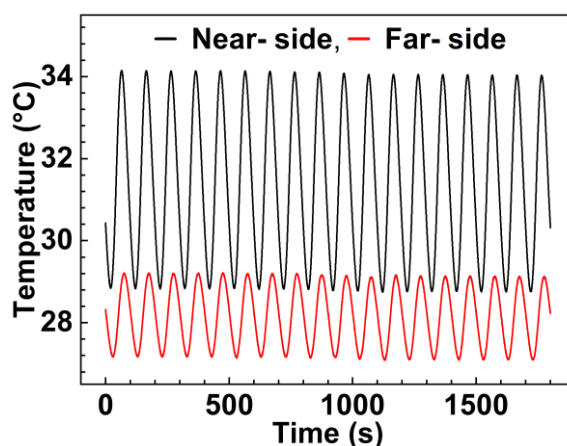

Figure S11. Near-side and far-side temperature response of the thermoocuple when the input peak to peak sinusoidal voltage input to the heater is 7 V and frequency 10 mHz.

Furthermore, the measurement accuracy utilizing the Angstrom method was confirmed by measuring the thermal diffusivity of fused quartz, mica, and pure high-density polyethylene with a known thermal diffusivity. The measurement results agree well (<5% deviation) with the results reported in literature. Although measuring the thermal conductivity of thin films can be difficult, the Angstrom method is a tried-and-true approach that has been used to measure the thermal conductivity of a variety of materials, including thermoelectric films.[1,6–8]

Supplementary Note 12. Machine learning and Bayesian optimization methods

Data preparation: In this work, we developed a machine learning framework that integrates Gaussian process regression (GPR), support vector machine (SVM), and BO to maximize the TE power factor while maintaining printability.

The GPR model captures the underlying relationships of the data through a kernel function and provides the probabilistic prediction for the power factors based on inputs. The inputs and output are standardized with zero mean and unit variance, ensuring that the model treats all variables equally. The kernel function in this work is given by:

$$K(\boldsymbol{x}, \boldsymbol{x}_* | \boldsymbol{\theta}) = constant^2 \times K_{\text{Matérn}}(\boldsymbol{x}, \boldsymbol{x}_* | \boldsymbol{l}, \nu) + \sigma^2,$$

$$K_{\text{Matérn}}(\boldsymbol{x}, \boldsymbol{x}_* | \boldsymbol{l}, \nu) = \frac{1}{\Gamma(\nu) 2^{\nu-1}} \left(\frac{\sqrt{2\nu}}{\boldsymbol{l}} d(\boldsymbol{x}, \boldsymbol{x}_*) \right)^\nu K_\nu \left(\frac{\sqrt{2\nu}}{\boldsymbol{l}} d(\boldsymbol{x}, \boldsymbol{x}_*) \right)$$

where $\boldsymbol{\theta}$ includes constant term $constant^2 = 0.907^2$, length scale $\boldsymbol{l}$, smoothness parameter for the Matern kernel ν and σ^2 is the noise level for the white noise. This kernel provides GPR flexibility and the ability to model complex data relationships. Within the Matérn kernel, the Euclidean distance $d(\cdot)$ is computed, utilizing the modified Bessel function $K_\nu(\cdot)$, and the gamma function $\Gamma(\cdot)$ for its calculations. The length scale $\boldsymbol{l}$, [1.86,4.25,5,5],influences how changes in the input space (TE particle loading, additive concentrations, filament spacing, standoff distance) affect the correlation between outputs. The smoothness parameter ν controls the smoothness of the resulting function, with $\nu = 1.5$ providing a balance between smoothness and flexibility, allowing the model to capture complex relationships in the data. $\sigma^2 = 0.102^2$ accounts for noise in the dataset. The GPR model utilizes this complex kernel to describe a joint multivariate Gaussian distribution between training data and prediction points. This distribution is described by mean function $m(\cdot)$, and covariance matrices derived from the kernel with the training data $\boldsymbol{X}$ and prediction point $\boldsymbol{x}_*$, denoted by:

$$\begin{bmatrix} f(X) \\ f(\boldsymbol{x}_*) \end{bmatrix} \sim N \left(\begin{bmatrix} m(X) \\ m(\boldsymbol{x}_*) \end{bmatrix}, \begin{bmatrix} K(X,X) & k(X,\boldsymbol{x}_*) \\ k(\boldsymbol{x}_*,X) & k(\boldsymbol{x}_*,\boldsymbol{x}_*) \end{bmatrix} \right)$$

From this distribution, the prediction means of the power factor $\mu_*(\boldsymbol{x}_*)$ for a given set of input conditions, $\boldsymbol{x}_*$, and prediction's uncertainty $\sigma_*(\boldsymbol{x}_*)$ can be calculated analytically.

$$\mu_*(\boldsymbol{x}_*) = E(f(\boldsymbol{x}_*) \mid \boldsymbol{y}) = m(\boldsymbol{x}_*) + k(\boldsymbol{x}_*,X)[K(X,X) + \sigma^2 I]^{-1}(\boldsymbol{y} - \boldsymbol{m}(X))$$

$$\sigma_*(\boldsymbol{x}_*) = \text{Var}(f(\boldsymbol{x}_*) \mid \boldsymbol{y}) = k(\boldsymbol{x}_*,\boldsymbol{x}_*) - k(\boldsymbol{x}_*,X)[K(X,X) + \sigma^2 I]^{-1}k(X,\boldsymbol{x}_*))$$

SVM: While GPR provides us with a probabilistic understanding and predictive power regarding the power factor, SVM models operate in parallel, focusing on the printability constraints in the optimization process. Two SVM models, filament $g_f(\boldsymbol{x})$ and surface roughness $g_r(\boldsymbol{x})$, are used after the first round to restrict the search space using the printability metrics.

$$g(x) = w^{\mathrm{T}}K(x) + b$$

where w contains the coefficients of the data, indicating the importance of each feature in determining the position of the decision boundary. b is the bias term that offsets the hyperplane from the origin to optimize class separation. By identify the hyperplane of the decision boundary, the problem become an optimization problem:

$$\min_{w,b,\zeta} \frac{1}{2}w^{\mathrm{T}}w + D\sum_{i=1}^{n}\zeta_i$$

where D is the penalty term, acting as the reciprocal of a regularization parameter, balancing the trade-off between the misclassification of training examples and the simplicity of the decision surface. ζ_i represents the distance from the misclassified samples to the correct hyperplane. Details of the SVM methodology can be found in references.[9–11]

For the Filament SVM, the linear kernel, $K(x, x_*) = x^{\mathrm{T}}x_*$ is used, and for surface roughness SVM, a radial basis function (RBF) kernel $K(x, x_*) = exp(-\gamma \parallel x - x_* \parallel^2)$ is used, where γ determines the impact of individual training samples on the model. The RBF kernel maps the input feature vectors into a higher-dimensional space, creating more flexibility to find a linear hyperplane in the new space. The SVM's outputs are calibrated by fitting a sigmoid function, enabling them to approximate probabilities. The output probability $\mathbb{P}(\cdot)$ for experimental condition quantifies the model's confidence in the sample's printability.

BO: Expected improvement (EI) is a statistical metric that quantifies the anticipated enhancement in the target function, $f(x)$, with respect to the predictive distribution provided by GPR model. More specifically, EI balanced exploration and exploitation by capturing the mean value of the improvement that each new test point might offer over the best result we have obtained so far. EI at point x_* is calculated $\mathrm{EI}(x) = \mathbb{E}[\max{(f(x_*) - f(x^+), 0}]$, where x^+ is the best observation in the current dataset. In our context, it is the best power factor achieved. Since GP provides the distribution over functions, $f(x_*)$ is normal distribution with mean $\mu_*(x_*)$ and variance $\sigma_*(x_*)$. EI can be calculated analytically under the Gaussian assumption:

$$\mathrm{EI}(x_*) = \begin{cases} (\mu_*(x_*) - f(x^+) - \xi)\Phi(z(x_*)) + \sigma_*(x_*)\phi(z(x_*)), & \sigma_*(x_*) > 0 \\ 0, & \text{otherwise} \end{cases}$$

$$z(x_*) = \begin{cases} \dfrac{(\mu_*(x_*) - f(x^+) - \xi)}{\sigma_*(x_*)}, & \sigma_*(x_*) > 0 \\ 0, & \text{otherwise} \end{cases}$$

where ξ is a positive number to encourage exploration, Φ and ϕ are the cumulative density function (CDF) and probability density function (PDF) of the standard normal distribution.

After the first round of the power factor's improvement, we form a constrained EI to effectively narrow down the search region, maintaining an acceptable printability of the material while maximizing the power factor. The constrained BO includes two SVM models alongside EI to formulate an Expected Improvement with Constraints (EIC), which can be represented as:

$$\text{EIC}(\boldsymbol{x}_*) = \text{EI}(\boldsymbol{x}_*) \times \mathbb{P}(z_f(\boldsymbol{x}_*) = 1) \times \mathbb{P}(z_r(\boldsymbol{x}_*) = 1)$$

where $\mathbb{P}$ is the probability that the constrained is satisfied. Iteratively, as new experiments are continuously generated and added to the dataset, the model can be more precise and robust in the prediction. The entire workflow is shown in **Figure S12**.
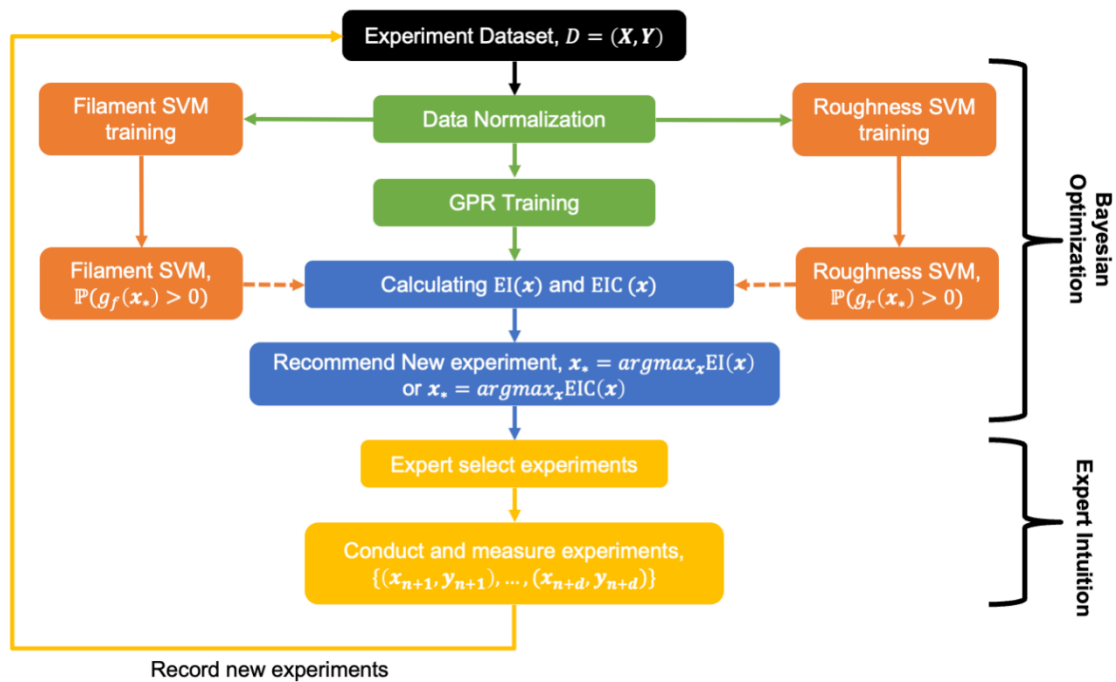

Figure S12. The proposed workflow integrates BO and Expert intuition. This process starts with the initial experiment dataset comprising 15 experiments. The overall procedure: GPR model training (green box), SVM models (orange box), the computation of EI and EIC (blue box), and new experiments candidates' selection (yellow box). Each optimization round results in conducting three experiments. The recorded outputs of these experiments feed into the subsequent iteration to refine the decision-making process.

Supplementary Note 13. The effects of X-gum concentration on the structure's porosity

Figure S13 shows the microstructures of printed TE samples with different X-gum concentrations. When the particle loadings are the same, a higher X-gum concentration always induces a higher porosity.
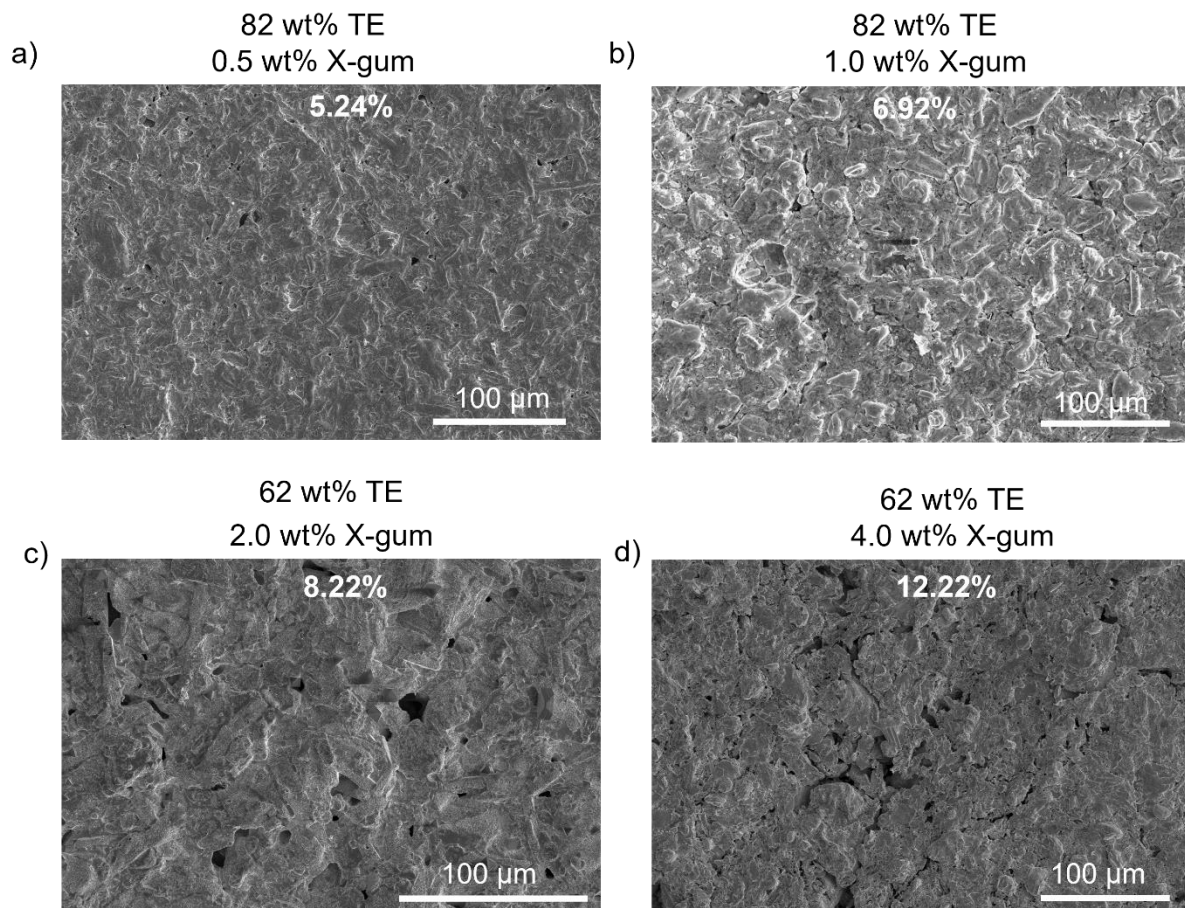

Figure S13. The effects of X-gum concentration on the structure's porosity.

References

[1]   T. Varghese, C. Dun, N. Kempf, M. Saeidi-Javash, C. Karthik, J. Richardson, C. Hollar, D. Estrada, Y. Zhang, *Adv Funct Mater* **2020**, *30*, 1.

[2]   S. E. Yang, F. Kim, F. Ejaz, G. S. Lee, H. Ju, S. Choo, J. Lee, G. Kim, S. ho Jung, S. Ahn, H. G. Chae, K. T. Kim, B. Kwon, J. S. Son, *Nano Energy* **2021**, *81*, 105638.

[3]   B. Chen, M. Kruse, B. Xu, R. Tutika, W. Zheng, M. D. Bartlett, Y. Wu, J. C. Claussen, *Nanoscale* **2019**, *11*, 5222.

[4]   C. Ou, *Cambridge University* **2020**.

[5]   D. H. Maylotte, P. G. Kosky, J. P. Gallo, *International Communications in Heat and Mass Transfer* **1999**, *26*, 1061.

[6]   M. Saeidi-Javash, K. Wang, M. Zeng, T. Luo, A. W. Dowling, Y. Zhang, *Energy Environ Sci* **2022**, *15*, 5093.

[7]   F. Kim, B. Kwon, Y. Eom, J. E. Lee, S. Park, S. Jo, S. H. Park, B. S. Kim, H. J. Im, M. H. Lee, T. S. Min, K. T. Kim, H. G. Chae, W. P. King, J. S. Son, *Nat Energy* **2018**, *3*, 301.

[8]   J. Huang, R. B. Ambade, J. Lombardo, B. Brooks, A. Poosapati, P. Banerjee, M. Saeidi-Javash, Y. Zhang, D. Madan, *Appl Mater Today* **2024**, *37*, 102116.

[9]   R. M. Neal, *Pattern Recognition and Machine Learning*, **2007**.

[10]   F. Michaud, M. Lamas, U. Lugrís, J. Cuadrado, *J Neuroeng Rehabil* **2021**, *18*, 199.

[11]   L. Buitinck, G. Louppe, M. Blondel, F. Pedregosa, A. Mueller, O. Grisel, V. Niculae, P. Prettenhofer, A. Gramfort, J. Grobler, R. Layton, J. Vanderplas, A. Joly, B. Holt, G. Varoquaux, *ArXiv* **2013**, 1.